



Isomeric acceptors incorporation enables 18.1% efficiency ternary organic solar cells with reduced trap-assisted charge recombination

Jie Lv^{a,b,c}, Qianguang Yang^d, Wanyuan Deng^e, Haiyan Chen^d, Manish Kumar^f, FuQing Zhao^d, Shirong Lu^{a,*}, Hanlin Hu^{c,*}, Zhipeng Kan^{b,*}

^a Department of Material Science and Technology, Taizhou University, Taizhou 318000, China

^b Center on Nano Energy Research, Guangxi Colleges and Universities Key Laboratory of Blue Energy and Systems Integration, Carbon Peak and Neutrality Science and Technology Development Institute, School of Physical Science & Technology, Guangxi University, Nanning 530004, China

^c Hoffmann Institute of Advanced Materials, Shenzhen Polytechnic, 7098 Liuxian Boulevard, Shenzhen 518055, China

^d Chongqing Institute of Green and Intelligent Technology, Chinese Academy of Sciences, Chongqing 400714, China

^e Institute of Polymer Optoelectronic Materials and Devices, State Key Laboratory of Luminescent Materials and Devices, South China University of Technology, Guangzhou 510641, China

^f Pohang Accelerator Laboratory, Pohang University of Science and Technology, Pohang, 37673, South Korea

ARTICLE INFO

Keywords:

Organic solar cells
Surface energy
Miscibility
Ternary
Trap density

ABSTRACT

The donor–acceptor miscibility is one of the most critical factors in controlling the active layer morphologies with multiple components. However, how to practically select the third component with the desired miscibility for efficient ternary organic solar cells remains unresolved. Herein, we demonstrate that the surface energy of thin films could be manipulated by altering the weight ratios of the isomeric acceptors in the blend films and, therefore, the regulation of donor–acceptor miscibility. When the acceptor weight ratio (M–Cl:O–Cl) is 1:0.3, low miscibility ($\chi = 5.43 \times 10^{-2}$) with PM6 is achieved, and the power conversion efficiency of organic solar cells composed of PM6:M–Cl (17.1%) is enhanced to 18.1% (PM6:M–Cl:O–Cl). The increased power conversion efficiency resulted from the surface energy-driven active layer morphology and donor–acceptor phase separations, associated with the significantly lower energetic disorder, trap density, and thus reduced free charge recombination. Our findings underline the significance of the isomeric approach to managing the blend film surface energy and, therefore, the donor–acceptor miscibility for improving the device performance, providing guidelines for the fabrication of high-performed ternary OSCs and material designs.

1. Introduction

Solution-processed bulk-heterojunction (BHJ) organic solar cells (OSCs) have attracted considerable attention owing to their simple fabrication process, lightweight, semitransparency, easy fabrication into flexible and large-area devices, etc. [1–4]. In the past few years, the power conversion efficiency (PCE) of single junction OSCs has reached 19%, and the PCE of tandem OSCs has reached 20% with the immense efforts in photovoltaic material designs, device engineering, and device physics [5–8]. These results gradually close the gap with the inorganic photovoltaic solar cells. However, the radiative/non-radiative recombination loss in OSCs are severe than those in their inorganic counterparts. Specifically, using the BHJ active layer can cause energy level bending at the donor/acceptor interfaces and isolated donor or acceptor

phase, resulting in substantial trap-assisted and bimolecular charge recombination [9–12]. Therefore, reducing the associated recombination loss is essential in further enhancing the PCE [13].

One of the straightforward ways to suppress the charge recombination was the active layer morphology optimization via processing solvent additive [14–18], solvent vapor annealing [19–22], and thermal annealing prior/after the electrode deposition [23–27]. The thin film morphology can be tuned with such treatments due to the solubility differences and the altered aggregation tendencies of the selected donor–acceptor pair. As a result, the exciton dissociation [28–30], charge transport, and collection efficiency can be improved [31,32], leading to reduced nongeminate recombination [7,32,33]. Due to the interpenetrating and bi-continuous donor/acceptor network in the BHJ film, trap states usually lead to severe trap-assisted charge

* Corresponding authors.

E-mail addresses: lushirong@cigit.ac.cn (S. Lu), hanlinhu@szpt.edu.cn (H. Hu), kanzhipeng@gxu.edu.cn (Z. Kan).

<https://doi.org/10.1016/j.cej.2023.142822>

Received 13 January 2023; Received in revised form 1 April 2023; Accepted 4 April 2023

Available online 6 April 2023

1385-8947/© 2023 Elsevier B.V. All rights reserved.

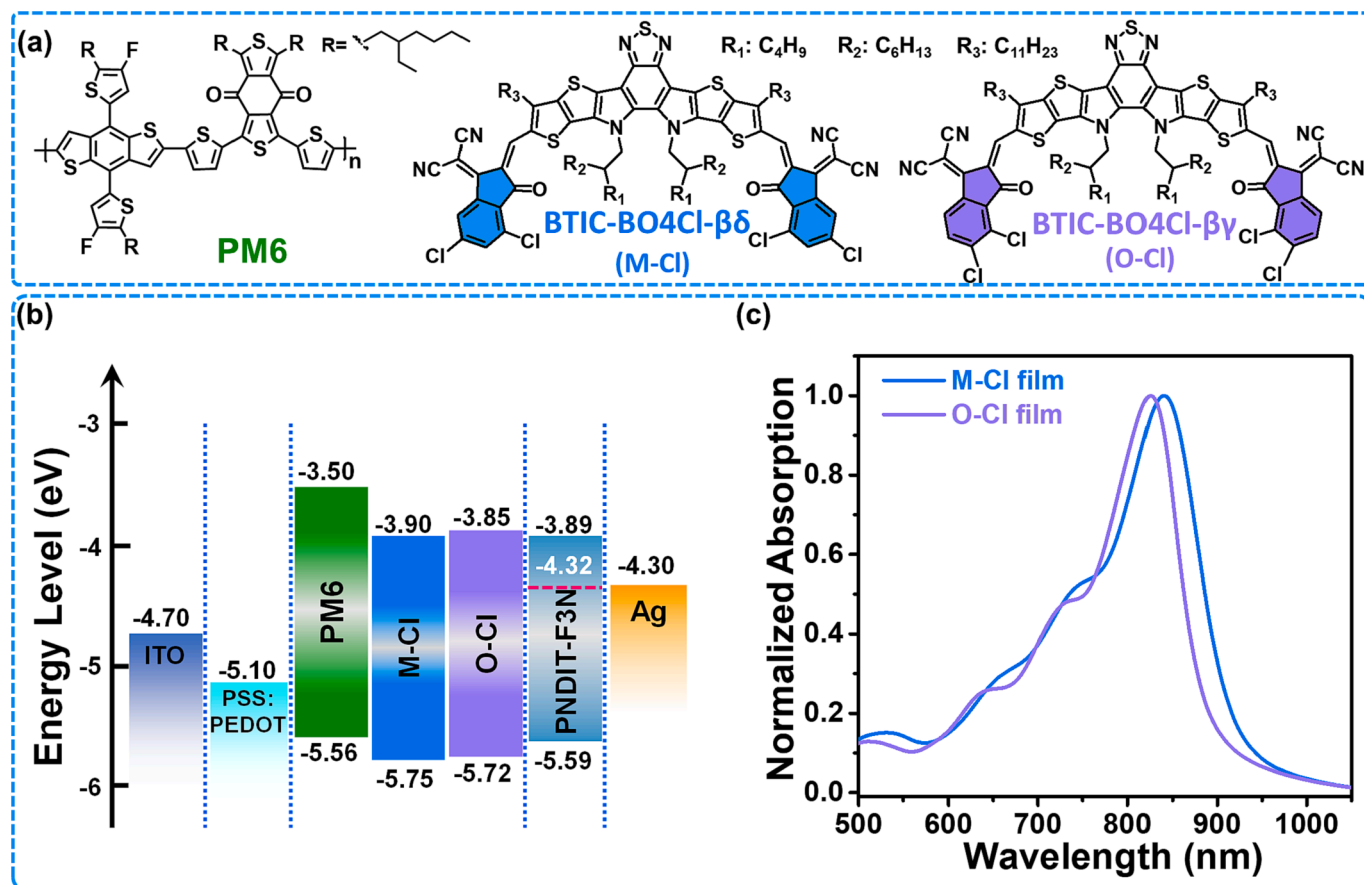


Fig. 1. (a) Molecular structures of the donor (PM6) and acceptors (M–Cl and O–Cl). (b) Energy level diagrams of ITO, PEDOT:PSS, PM6, M–Cl, O–Cl, PNDIT-F3N, and Ag. (c) Normalized UV–vis absorbance spectra of M–Cl and O–Cl in thin films.

recombination loss [34–36]. A molecular doping strategy is often used to minimize the trap states. By adding a tiny amount of n-type doping material or Lewis Acid to compensate for the defects in the active layer, the trap states could be successfully filled and enhance the device performance due to improved charge transport performance and reduced charge recombination [37–39]. Besides the mentioned methods, OSCs with multiple materials in the active layer, especially ternary OSCs with a third component, were demonstrated to be an effective way to tune the active layer microstructures and thus reduce charge recombination [40]. For instance, the use of volatilizable solid additives was reported as a practical way to optimize the crystalline features of the active layer, which enhanced the charge extraction and suppressed the charge recombination progressively, leading to a PCE of 19.05% [41]. The double-fibril network was realized based on a ternary donor–acceptor morphology with minimized energy losses and increased exciton diffusion length to reduce charge recombination, attaining a PCE of 19.6% [33]. Though the PCE of ternary OSCs has been improved dramatically, a successful third component selection and its impact on the active layer morphology are still investigated by trial and error. It is proposed that the surface energy of neat materials in the thin film could be one of the critical parameters to screen the third component [29,30,42,43], which determines the miscibility of the donor–acceptor materials. When a cascade arranged surface energy of the host donor–acceptor and the third component is realized, the donor–acceptor network in the active layer could be effectively optimized because of the miscibility caused interaction of the three components [42,44–46]. However, aside from the new chemical structure design and synthesis, how to effectively tune the surface energy of the materials is rarely discussed.

In this work, we systematically investigated surface energy control by utilizing isomeric acceptors BTIC-BO4Cl-βδ and BTIC-BO4Cl-βγ with

terminal Cl substitution positions at meta and ortho positions developed by Lai et al., paired with polymer donor PM6 [47]. To simplify the description of acceptor materials, BTIC-BO4Cl-βδ and BTIC-BO4Cl-βγ are abbreviated as M–Cl and O–Cl, respectively. We could tune the surface energy of thin films composed of M–Cl and O–Cl by altering their weight ratios, thereby changing the miscibility with PM6. Additionally, the PCE of OSCs composed of PM6:M–Cl (17.1%) was enhanced to 18.1% when ca. 30% (in weight) of O–Cl was added as a third component. The apparent increased PCE resulted from the miscibility-driven active layer morphology and donor–acceptor phase separations, associated with the significantly reduced energetic disorder, trap density, and free charge recombination. Our results reveal that the isomer materials approach is simple yet effective in tuning the surface energy (miscibility) for fabricating efficient ternary OSCs.

2. Results and discussion

Fig. 1a shows the molecular structures of PM6, M–Cl, and O–Cl, where M–Cl and O–Cl are isomers of each other with the same BTP core framework but with *meta*-chloro-substituted and *ortho*-chloro-substituted. Fig. 1b depicts the energy levels diagram of the materials used in the active layer determined by cyclic voltammetry measurements. The lowest unoccupied molecular orbital (LUMO) and the highest occupied molecular orbital (HOMO) levels of PM6 are –3.50 eV and –5.56 eV, respectively. The LUMO/HOMO energy of M–Cl is –3.90/–5.75 eV, slightly deeper than those of O–Cl (–3.85/–5.72 eV). The energy offset between the donor and acceptors indicates that the OSCs composed of M–Cl and O–Cl paired with PM6 could work properly. Fig. 1c presents normalized UV–vis absorbance spectra of M–Cl and O–Cl in neat films. The absorption maximum of M–Cl is 840.5 nm, which is

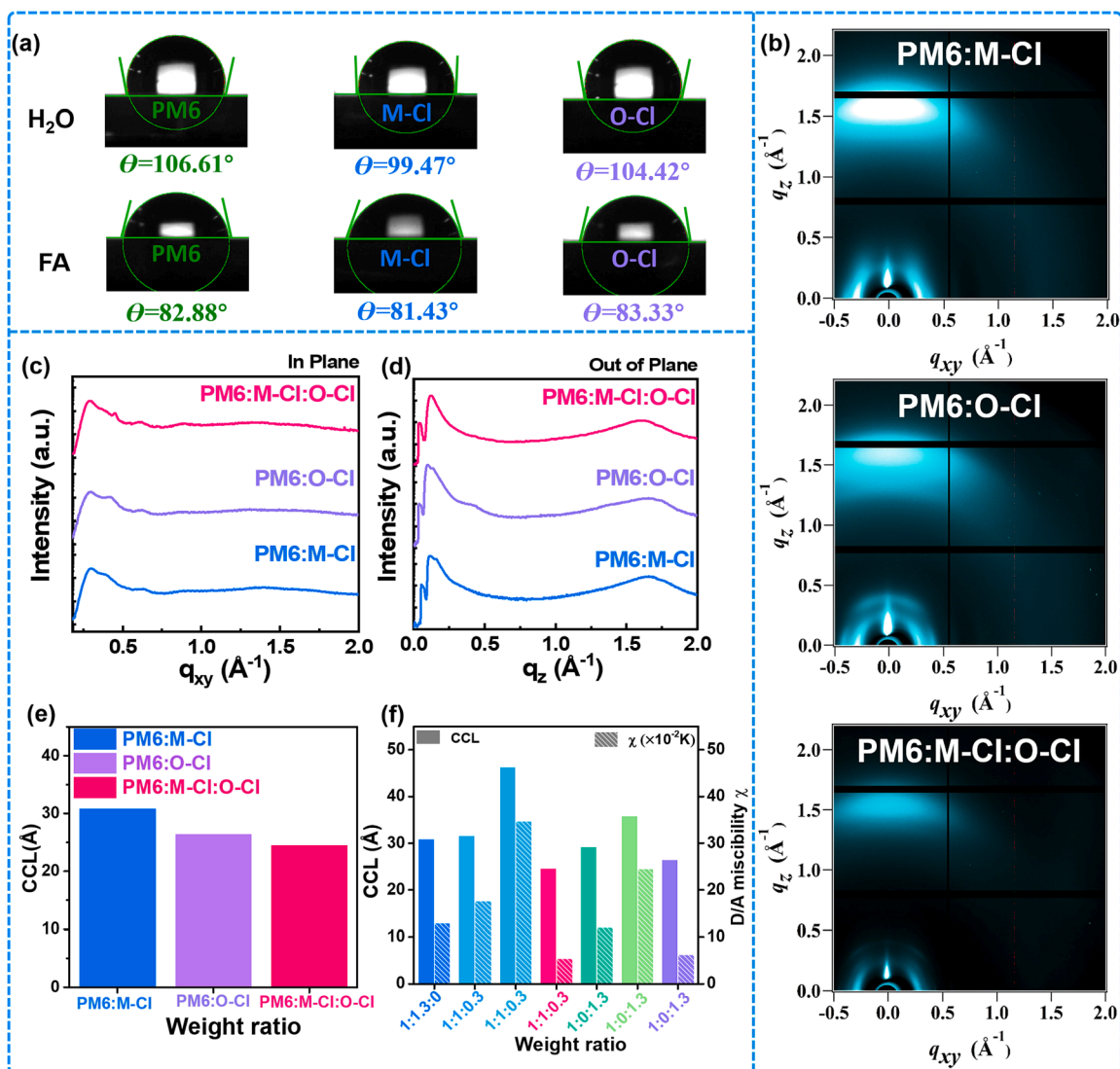


Fig. 2. (a) The Deionized water and formamide (FA) contact angles of the pristine PM6, M-Cl, and O-Cl. (b) 2D GIWAXS patterns of thin films of PM6:M-Cl, PM6:O-Cl, and PM6:M-Cl:O-Cl; (c) and (d) Corresponding GIWAXS intensity profiles along the in-plane and out-of-plane directions of PM6:M-Cl, PM6:O-Cl, and PM6:M-Cl:O-Cl; (e) CCL in the out-of-plane π - π peak of the PM6:M-Cl, PM6:O-Cl and PM6:M-Cl:O-Cl films; (f) The Relationship between CCL of (010) π - π stacking and D/A miscibility parameter χ at different donor/acceptor ratios.

red-shifted by 15 nm compared with that of O-Cl (825.6 nm).

To get the surface energy (γ) of the materials used in thin films, we performed contact angle measurements with water and formamide (FA). The contact angle and γ are summarized in Table S1, and the pictures are presented in Fig. 2a. As listed in Table S2, the γ calculated for the acceptor blends (M-Cl:O-Cl) varies with the M-Cl and O-Cl weight ratios. The minimum γ of 26.63 mJ m⁻² is obtained when the weight ratio of M-Cl and O-Cl is 1:0.3. With the surface energy attained, the miscibility parameter χ is calculated based on the Flory-Huggins theory [30,43,48,49]. The detailed calculation method is provided in the supporting information. The χ of PM6/M-Cl is 12.89×10^{-2} K, which is larger than that of PM6/O-Cl (χ is 6.21×10^{-2} K). The larger χ is the driving force of donor-acceptor phase separation in the film [30], reflecting the relatively small degree of donor-acceptor miscibility, which may lead to inappropriate phase separation. When the M-Cl and O-Cl are combined with a weight ratio of 1:0.3, a χ of PM6 and M-Cl:O-Cl with the value of 5.43×10^{-2} K is derived, indicating a more considerable extent of donor-acceptor miscibility in this ternary film compared with those of the binary counterparts. We speculate that the change of miscibility of the acceptor blends M-Cl:O-Cl with the PM6

donor is due to the adjustment of the film crystallinity phases. Therefore, we turned to check the crystalline features in the thin films.

Grazing incidence wide-angle X-ray scattering (GIWAXS) was carried out to study the molecular packing and orientation in the thin films. The 2D GIWAXS patterns of the ternary blend films with different M-Cl:O-Cl components are presented in Fig. S2. The in-plane (IP) and out-of-plane (OOP) scattering profiles of the thin films are shown in Fig. 2c-d and Fig. S3, and the detailed structural parameters are summarized in Tables S5 and S6. In the OOP direction (Fig. S3b), except that the 1:1:0.3 film exhibits a weaker lamellar scattering peak, multiple lamellar peaks were observed at other weight ratios, indicating that 1:1:0.3 blend film has more order molecular stacking. The ternary system (010) π - π stacking crystallinity shows a noticeable difference (Fig. S2 and Fig. S3b). The 1:1:0.3 blend film shows the weakest (010) π - π stacking peak at $q_z \approx 1.606$ Å⁻¹, with a CCL = 24.6 Å, the π - π stacking peaks of 1:1.2:0.1, 1:1.1:0.2, 1:0.8:0.5 and 1:0.2:1.1 are located at $q_z \approx 1.667$ Å⁻¹, $q_z \approx 1.667$ Å⁻¹, $q_z \approx 1.641$ Å⁻¹, and $q_z \approx 1.671$ Å⁻¹ with CCLs of 31.6 Å, 46.3 Å, 27.0 Å, and 30.7 Å, respectively. Furthermore, compared with PM6:M-Cl and PM6:O-Cl films, the (010) π - π stacking crystallinity of PM6:M-Cl:O-Cl (1:1:0.3) blend film is weaker than binary system (q_z

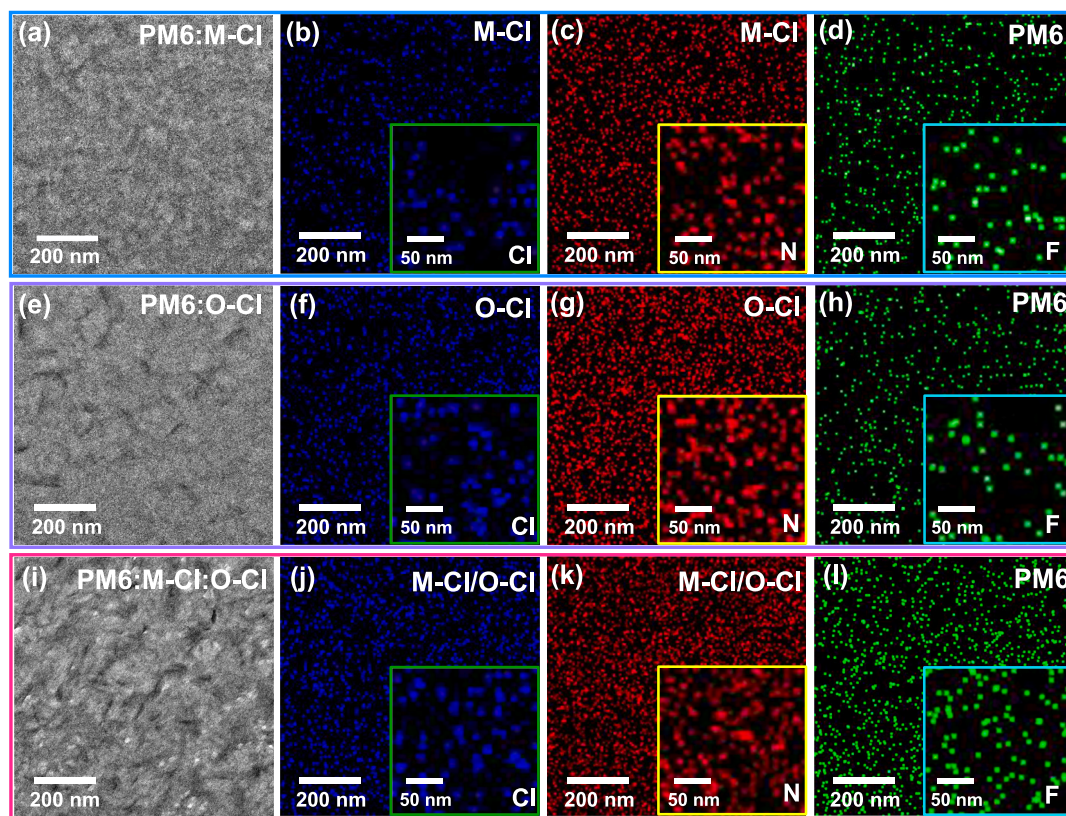


Fig. 3. TEM images of high angle annular dark field (HAADF) in scanning-transmission (STEM) mode with X-Ray spectroscopy (EDS) mapping for (a) PM6:M-Cl, (e) PM6:O-Cl, and (i) PM6:M-Cl:O-Cl. (b), (f), and (j) are the Cl element distributions of the acceptor in the blend film, which are shown in blue. (c), (g), and (k) are the N element distribution of the acceptor in the blend film, which are shown in red. (d), (h), and (i) are the F element distributions of the donors in the blend films and are shown in green.

$\approx 1.671 \text{ \AA}^{-1}$ with CCL = 30.9 \AA for PM6:M-Cl and $q_z \approx 1.623 \text{ \AA}^{-1}$ with CCL = 26.5 \AA for PM6:O-Cl as shown in Fig. 2b and 2d. We noticed a relationship between crystallinity and miscibility parameter χ in blend films, as presented in Fig. 2f. It is observed that high crystalline films are associated with large χ , indicating poor donor-acceptor miscibility and excessive donor-acceptor phase separation. Compared with the binary films of PM6:O-Cl and PM6:M-Cl, the ternary film with M-Cl:O-Cl ratio of 1:0.3 shows lower crystallinity and good donor-acceptor miscibility, suggesting that the addition of O-Cl influenced the donor-acceptor phase segregations in the thin film. To unveil the effect of O-Cl on the donor-acceptor distribution in the thin film, we performed atomic force microscopy (AFM) and transmission electron microscopy (TEM) measurements on PM6:M-Cl, PM6:O-Cl, and PM6:M-Cl:O-Cl blend films.

As displayed in AFM height images (Fig. S4a-c), the blend film of PM6:M-Cl, PM6:O-Cl, and PM6:M-Cl:O-Cl (1:1:0.3) demonstrates a similar root mean square roughness (Rq) values of 0.903 nm, 0.915 nm, and 0.927 nm, respectively, which is conducive to forming a well ohmic contact with the electrode. Besides, when compared with the phase images of PM6:M-Cl and PM6:O-Cl, PM6:M-Cl:O-Cl (1:1:0.3) demonstrates a more straightforward and enhanced fiber network with more uniform and orderly network distribution (Fig. S4g-i), which could effectively contribute to the charge transport. The TEM images (Fig. 3a, 3e, and 3i) show the different donor-acceptor networks of the PM6:M-Cl, PM6:O-Cl, and PM6:M-Cl:O-Cl (1:1:0.3) films. The phase-separated network of PM6:O-Cl film shows non-uniform phase-separated morphologies and domain sizes, which is attributed to the donor/acceptor's good miscibility ($\chi = 6.21 \times 10^{-2} \text{K}$). But this non-uniformity is not conducive to charge transport and easily leads to lower FF due to space charge accumulation and bimolecular charge recombination [13,29,50,51]. As to the TEM images of PM6:M-Cl, there is a compact and larger domain size ($\chi = 12.89 \times 10^{-2} \text{K}$, a larger χ value causes phase

aggregation), which may be achieved efficient charge carrier mobilities on a local scale. However, due to the donor/acceptor miscibility adjustment in blend films, the phase-separated D/A network of PM6:M-Cl:O-Cl (1:1:0.3) (Fig. 3i) was significantly optimized, resulting in a suitable domain size and an ordered network structure. This observation could be attributed to the introduction of O-Cl, which induces the redistribution of donor/acceptor.

Moreover, we characterized the donor-acceptor distribution by high-angle annular dark field (HAADF) in scanning-transmission (STEM) mode with Energy dispersive spectrometry (EDS) mapping. In this measurement, we monitored the atoms of chlorine (Cl) and nitrogen (N) in the acceptor phase and traced the atom of fluorine (F) in the donor phase. Through the quantitative analysis of F, Cl and N presented in Fig. 3 (additional information in Fig. S5 and Table S7), we observe that the atomic percentages of Cl and N atoms in the PM6:M-Cl film are 81.12% and 11.63%, respectively, which are less than those of the PM6:O-Cl film (82.71% and 12.16% of N and Cl, respectively). Contrastingly, the atomic percentage of F in the PM6:M-Cl films is 7.25%, greater than 5.13% in the PM6:O-Cl films. These observations suggest that there is less acceptor distribution and more donor distribution in the PM6:M-Cl system, whereas, in the PM6:O-Cl layer, there is more acceptor distribution and less donor distribution (Fig. 3b-d). At the same time, we notice that in the PM6:M-Cl:O-Cl film, the atomic percentages of N, Cl, and F are 82.06%, 11.4%, and 6.52%, respectively. Though the atomic ratios are similar, the counts of Cl and N atoms in the same bulk volume are higher than those of the PM6:M-Cl and PM6:O-Cl films and are twice as high as the PM6:M-Cl blend film, while the counts of F atoms are between the films of PM6:M-Cl and PM6:O-Cl. This finding indicates that introducing O-Cl could actively regulate the distribution of the donor and acceptor phases, which maybe plays a critical role in further enhancing the charge transport and reducing charge

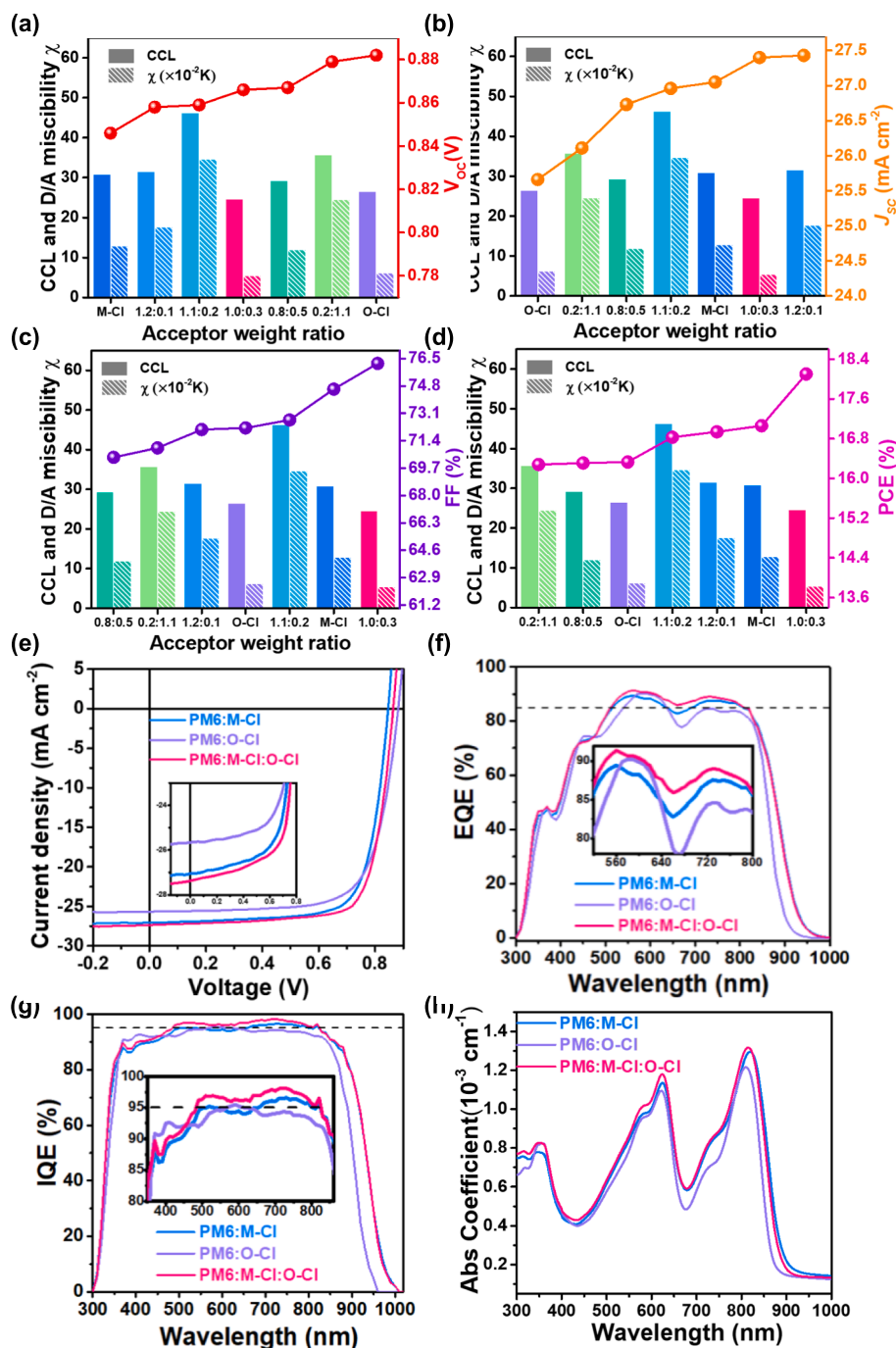


Fig. 4. The impact of CCL, D/A miscibility parameter χ , and acceptor blend (M-Cl:O-Cl) weight ratio on device parameters of (a) V_{OC} , (b) J_{SC} , (c) FF, and (d) PCE. (e) J - V characteristics of PM6:M-Cl, PM6:O-Cl, and PM6:M-Cl:O-Cl devices. (f) EQE spectra (Scale-up EQE spectra of 520–800 nm). (g) IQE spectra (Scale up IQE spectra of 360–850 nm). (h) The absorption coefficient spectra of PM6:M-Cl, PM6:O-Cl, and PM6:M-Cl:O-Cl films.

recombination.

To verify the effects of structural changes on the photovoltaic performance, we, therefore, fabricated OSCs composed of PM6:M-Cl:O-Cl with the ratio of 1:1:0.3 (in weight) and compared them with those containing PM6:M-Cl, PM6:O-Cl, and PM6:M-Cl:O-Cl with weight ratios other than 1:1:0.3. To clearly understand the change rule of photoelectric performance and the relationship with CCL, D/A miscibility parameter χ and acceptor blend (M-Cl:O-Cl) weight ratio, we plotted the relationship diagram drawn in the order of V_{OC} , J_{SC} , FF and PCE parameters from low to high, as shown in Fig. 4a ~ 4d. We observe four prominent features from these figures. First, the V_{OC} increases monotonously with the addition of O-Cl in the active layer, but it is not affected

by CCL and χ , and the maximum V_{OC} is achieved when the OSCs are composed of PM6:O-Cl, following a typical ternary blend alloy mode [45,52]; second, the changes of J_{SC} are complicated with the acceptor ratios, CCL, and χ ; third, the fill factor (FF) is inversely proportional to χ with the presence of O-Cl in the active layer; last, PCE has an obvious inverse correlation with CCL and χ . This system obtains high PCE values with low CCL and low χ (Fig. 4d). The high V_{OC} may result from the larger LUMO of O-Cl than that of M-Cl [53–56], whereas the changes of J_{SC} and FF are strongly related to the charge dynamics will be discussed in later sections. Consequently, strong correlations between the changes in CCL and χ at different receptor ratios and the device performance are established. Therefore, we propose that the surface energy governing the

Table 1

The photovoltaic parameters of OSCs with PM6:M-Cl, PM6:O-Cl, and PM6:M-Cl:O-Cl as the active layer. All data were obtained under the AM 1.5G (100mW cm⁻²) light source illumination.

Active layer D:A ratio (in wt%)	V _{OC} [V]	J _{SC} [mA cm ⁻²]	Calc. J _{SC} [mA cm ⁻²] ^a	FF [%]	PCE ^b [%]
PM6:M-Cl 1:1.3	0.846 (0.846 ± 0.053)	27.05 (27.01 ± 0.17)	26.95	74.6 (73.2 ± 1.4)	17.1 (16.7 ± 0.3)
PM6:O-Cl 1:1.3	0.882 (0.881 ± 0.004)	25.66 (25.58 ± 0.30)	25.28	72.2 (70.2 ± 1.6)	16.3 (15.8 ± 0.3)
PM6:M-Cl: O-Cl 1:1:0.3	0.866 (0.859 ± 0.006)	27.40 (27.22 ± 0.21)	27.29	76.2 (74.2 ± 1.3)	18.1 (17.4 ± 0.3)

a) Integrated J_{SC} from the EQE curves; b) The average parameters were calculated across 15 independent cells.

donor-acceptor miscibility could modulate the donor-acceptor phase separation.

The optimal device of PM6:M-Cl exhibits a V_{OC} of 0.846 V, a J_{SC} of 27.05 mA cm⁻², and an FF of 74.6%, leading to a PCE of 17.1%. In

comparison, the PCE of PM6:O-Cl is 16.3%, with a V_{OC} of 0.882 V, a J_{SC} of 25.66 mA cm⁻², and an FF of 72.2%. Specifically, the ternary devices obtain a champion PCE of 18.1%, with a V_{OC} of 0.866 V, J_{SC} of 27.40 mA cm⁻², and FF of 76.2%, outperforming the binary and other ternary counterparts. The J-V characteristics of best-performed binary and ternary devices are plotted in Fig. 4e. The photovoltaic parameters are summarized in Table 1, and it is observed that the V_{OC}, J_{SC}, and FF of the ternary device are significantly enhanced than those of the binary devices. More information on the device fabrication conditions and parameters is provided in Table S8 and Fig. S6.

Fig. 4f presents the EQE spectra of PM6:M-Cl, PM6:O-Cl, and PM6:M-Cl:O-Cl devices. The EQE curves of the PM6:M-Cl:O-Cl device is very similar to PM6:M-Cl in shape and co-exists in the spectral response range of 300–950 nm; however, the PM6:M-Cl:O-Cl device exhibits a stronger photon to electron response than that of the PM6:M-Cl device in the range of 520–788 nm, which contributes to the enhanced J_{SC}, this is consistent with the results of the absorption coefficient spectrum of the blend membrane (Fig. 4h). The EQE maximum of the PM6:M-Cl:O-Cl device is 91.36% at 560 nm, obviously higher than the PM6:M-Cl device of 89.43% at 560 nm, and the PM6:O-Cl device of 90.27% at 580 nm. Furthermore, in the ternary device of PM6:M-Cl:O-Cl, the EQE response of the donor and acceptor regions exceeded 85% in the range of

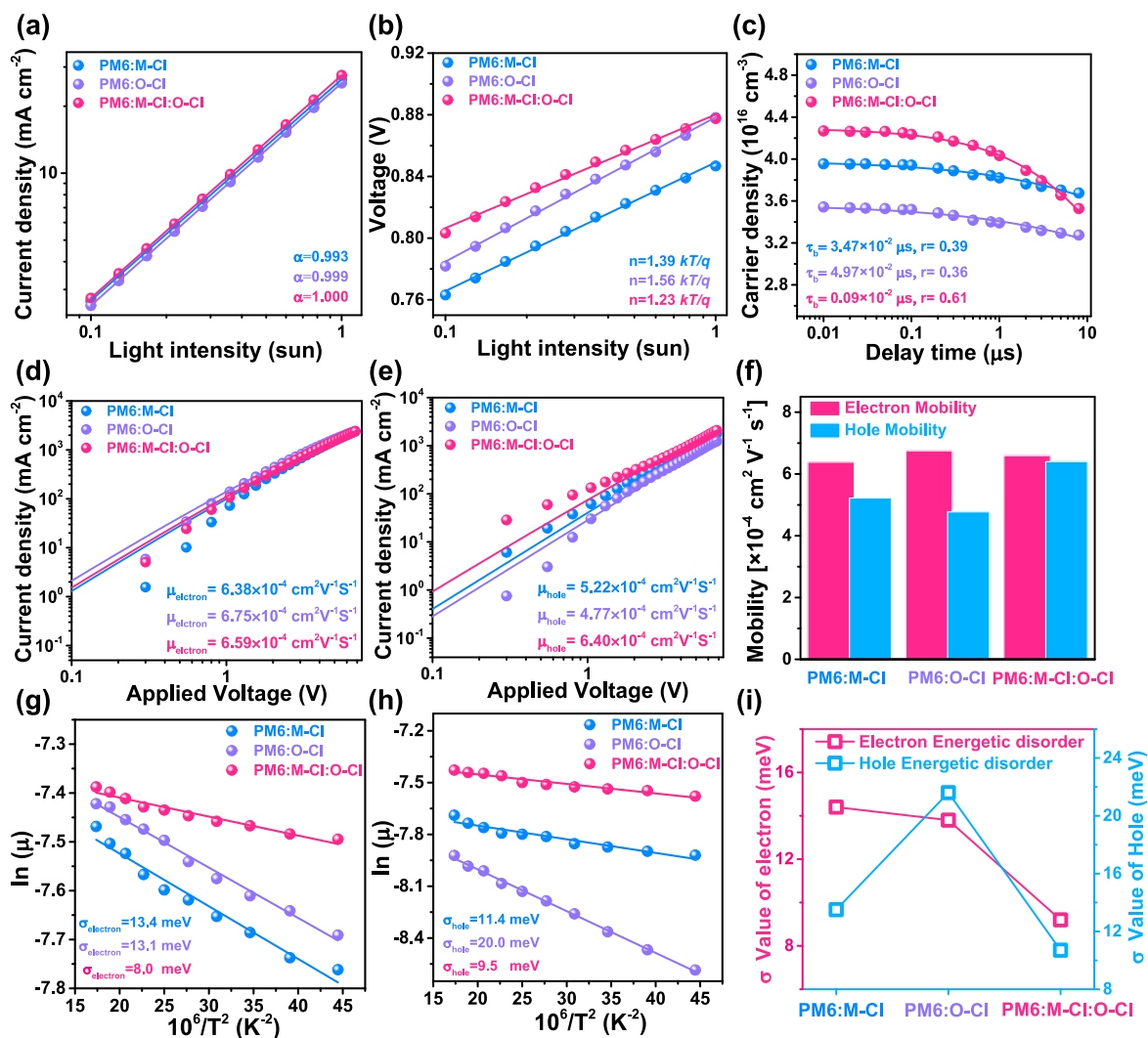


Fig. 5. (a) and (b) J_{SC} and V_{OC} dependence on the light intensity; (c) Carrier concentration decay plot calculated by integrating the transient photo-carrier current in Photo-CELIV curves of PM6:M-Cl, PM6:O-Cl and PM6:M-Cl:O-Cl devices; (d) and (e) Dark J-V curves of the OSCs: hole-only diodes and electron-only diodes, the solid lines are fit to the experimental data according to SCLC model; (f) Histogram of the electron and hole mobilities for PM6:M-Cl, PM6:O-Cl and PM6:M-Cl:O-Cl blends; (g) zero-field hole mobility μ_{0,h}, and (h) electron mobility μ_{0,e} versus (1000/T)², (i) Statistical comparison image of the electron and hole energy disorder.

520 nm to 810 nm, and the average EQE is 88.38%, significantly higher than PM6:M–Cl device of 86.57%, and PM6:O–Cl device of 84.41% (in Table S9). The J_{SC} values of the PM6:M–Cl, PM6:O–Cl, and PM6:M–Cl:O–Cl devices integrated from the EQE spectra are 26.95, 25.28, and 27.29 mA cm⁻², respectively, which are close to the J_{SC} values measured from the solar simulator (within a 0.3% error of PM6:M–Cl and PM6:M–Cl:O–Cl devices, within a 1.4% error of PM6:O–Cl device, Table 1).

To perceive the origin of the performance improvement in the ternary device, we tuned to check the reference and ternary devices' electrical and active layer morphological properties. First, we looked at the internal quantum efficiency (IQE) spectra. Unlike EQE, optical losses such as reflection and transmittance are excluded in the IQE spectra. Therefore, information on charge generation, recombination, and extraction could be qualitatively inferred from the IQE differences [57,58]. As depicted in Fig. 4g, the IQE of the PM6:M–Cl:O–Cl device is significantly enhanced in the range from 520 ~ 810 nm, with a maximum peak of 98.17% at 720 nm, which is higher than the PM6:M–Cl device of 96.57% at 730 nm and PM6:O–Cl device of 95.47% at 590 nm. The PM6:M–Cl:O–Cl device yields averaged IQE of 96.89% between 520 ~ 810 nm, whereas the same analysis leads to 95.29% and 94.25% of PM6:M–Cl and PM6:O–Cl devices, respectively. Overall, the higher IQE of the ternary blend implies better charge generation and extraction, which are beneficial for improving J_{SC} [57], and closely related to the carrier dynamics. Thus, more detailed carrier dynamics analysis and morphological characterizations have been performed.

The results mentioned above show that the addition of O–Cl directly influences the behavior of the free charge carriers in the devices; thereby, charge carrier dynamics are investigated in different ways. Firstly, incident light intensity-dependent J - V response and the recombination coefficient test are executed. Previous studies have reported that the bimolecular recombination losses could be qualitatively analyzed by employing short circuit current density and incident light intensity satisfied with a power law, i.e., $J_{SC} \propto I^\alpha$, fitting J_{SC} as a function of the incident light intensity plotted in log scales, α closer to unity represents better charge collection and less bimolecular recombination. The relationship between J_{SC} and incident light intensity is illustrated in Fig. 5a. From fitting the data of J_{SC} vs. light intensity, α values of 0.993, 0.999, and 1.00 were obtained for PM6:M–Cl, PM6:O–Cl, and PM6:M–Cl:O–Cl devices, respectively. The α values attained suggest that PM6:O–Cl and PM6:M–Cl:O–Cl devices are less affected by bimolecular charge recombination than PM6:M–Cl devices. On the other hand, the presence of trap-assisted charge recombination can be distinguished from the ideality factor n of the device. To estimate the n , V_{OC} as a function of the incident light intensity was measured, and the data followed the expression of $V_{OC} \propto nkT/q \ln(I)$, where n , k , T , and q are the ideality factor, Boltzmann constant, the temperature in Kelvin, and elementary charge, respectively. If n deviates from 1 (trap-free condition) [59], it indicates the presence of trap-assisted recombination. As fitted in Fig. 5b, the n values of PM6:M–Cl, PM6:O–Cl, and PM6:M–Cl:O–Cl devices resulted in 1.39, 1.56, and 1.23, indicating that the addition of O–Cl in the PM6:M–Cl:O–Cl device can notably reduce the trap density in the active layer.

To quantify the influence of O–Cl on bimolecular charge recombination and trap density in the devices, we performed delay time charge extraction with linearly increasing voltage (CELIV) measurements with pulse light. The charge density can be obtained by integrating the photo-CELIV current transient signals. Fig. S7 is the photo-CELIV current transient signals of PM6:M–Cl, PM6:O–Cl, and PM6:M–Cl:O–Cl devices, and Fig. 5c shows the charge density as a function of the delay time for the PM6:M–Cl, PM6:O–Cl and PM6:M–Cl:O–Cl devices. The charge density follows the dispersive bimolecular recombination model as shown below:

$$N(t) = \frac{N_0}{1 + \left(\frac{t}{\tau_b}\right)^r}$$

Table 2

Statistics of charge recombination-related parameters for PM6:M–Cl, PM6:O–Cl, and PM6:M–Cl:O–Cl devices.

Parameter	PM6:M–Cl	PM6:O–Cl	PM6:M–Cl:O–Cl
n_0 (cm ⁻³)	3.98×10^{16}	3.57×10^{16}	4.29×10^{16}
τ_b (μ s)	3.47×10^{-2}	4.97×10^{-2}	0.09×10^{-2}
r	0.39	0.36	0.61
μ_e ($\times 10^{-4}$ cm ² V ⁻¹ s ⁻¹)	6.38 ± 0.09	6.75 ± 0.69	6.59 ± 0.08
μ_h ($\times 10^{-4}$ cm ² V ⁻¹ s ⁻¹)	5.22 ± 0.26	4.77 ± 0.29	6.40 ± 0.71
μ_e/μ_h	1.22	1.42	1.03
σ_e (meV)	13.4	13.1	8.0
σ_h (meV)	11.4	20.0	9.5
V_{TFL} (Electron) V	0.226	0.196	0.148
V_{TFL} (Hole) V	None	0.324	None
Electron trap density (cm ⁻³)	3.89×10^{15}	3.37×10^{15}	2.55×10^{15}
Hole trap density (cm ⁻³)	Trap-free	5.58×10^{15}	Trap-free

where N is the carrier concentration, N_0 is the charge density at $t = 0$ and r is the time-independent parameter (r closes to 1, indicating nondispersive bimolecular recombination at room temperature), and τ_b is dispersive bimolecular recombination time constant related with trap density [60–63]. The PM6:M–Cl:O–Cl device exhibits an N_0 value of 4.29×10^{16} cm⁻³, larger than its PM6:M–Cl and PM6:O–Cl counterparts (3.98×10^{16} cm⁻³ and 3.57×10^{16} cm⁻³), in conformity to the high J_{SC} in the ternary device. The r values of the PM6:M–Cl, PM6:O–Cl, and PM6:M–Cl:O–Cl devices are 0.36, 0.39, and 0.61, as depicted in Table 2, suggesting that all the devices suffer from time-dependent bimolecular charge recombination and it is least dispersive in the ternary devices. The value of τ_b is 0.09×10^{-2} μ s for the PM6:M–Cl:O–Cl device, smaller than that for the PM6:M–Cl (3.47×10^{-2} μ s), and PM6:O–Cl device (4.97×10^{-2} μ s). The larger τ_b indicates more trap presence in the devices; therefore, the ternary devices indeed have less extent of traps than the other devices. These results demonstrate that ternary device can effectively control the density of trap states to enhance charge carrier transport, thereby improving the J_{SC} and enhancing the device's performance, which is in line with the aforementioned higher J_{SC} , EQE, and IQE response in the PM6:M–Cl:O–Cl device.

The hole and electron mobilities derived from the space-charge-limited-current (SCLC) model evaluated the charge transport properties. The hole-only devices are fabricated with the structure of ITO/PEDOT:PSS/active layer/MoO₃/Ag and electron-only devices with ITO/ZnO/PNDIT-F3N/active layer/PNDIT-F3N/Ag. The electron and hole mobility values are presented in Fig. 5d–f with the electron mobility and hole mobility statistics histogram of PM6:M–Cl, PM6:O–Cl, and PM6:M–Cl:O–Cl devices. The PM6:M–Cl device exhibits the electron mobility of 6.38×10^{-4} cm² V⁻¹ s⁻¹, but lower than the PM6:O–Cl device (6.75×10^{-4} cm² V⁻¹ s⁻¹). On the contrary, the hole mobility of PM6:M–Cl device is 5.22×10^{-4} cm² V⁻¹ s⁻¹, higher than the PM6:O–Cl device (4.77×10^{-4} cm² V⁻¹ s⁻¹). Nevertheless, the incorporation of O–Cl plays a positive role in the improvement of the hole and electron mobilities, and the electron mobility (6.59×10^{-4} cm² V⁻¹ s⁻¹) and hole mobility (6.40×10^{-4} cm² V⁻¹ s⁻¹) of the PM6:M–Cl:O–Cl device is improved compared with the PM6:M–Cl device. The higher and more balanced electron and hole mobilities ($\mu_h/\mu_e = 1.03$) could lead to the superior FF in the PM6:M–Cl:O–Cl devices (Fig. 5f and Table 2). Additionally, the hole and electron energy disorder (σ_h and σ_e) can be obtained from temperature-dependent mobility characterizations using the Gaussian disorder model (GDM), and the energetic disorder σ can be expressed as the following equation:

$$\mu_0 = \mu_\infty \exp \left\{ - \left(\frac{4}{9} \right) \left[\frac{\sigma^2}{(kT)^2} \right] \right\}$$

where k is the Boltzmann constant, T is the temperature, μ_0 is the zero-field mobility, and μ_∞ is the mobility at infinite temperature. Fig. 5g and Fig. 5h depict the zero-field electron and hole mobilities of PM6:M–Cl,

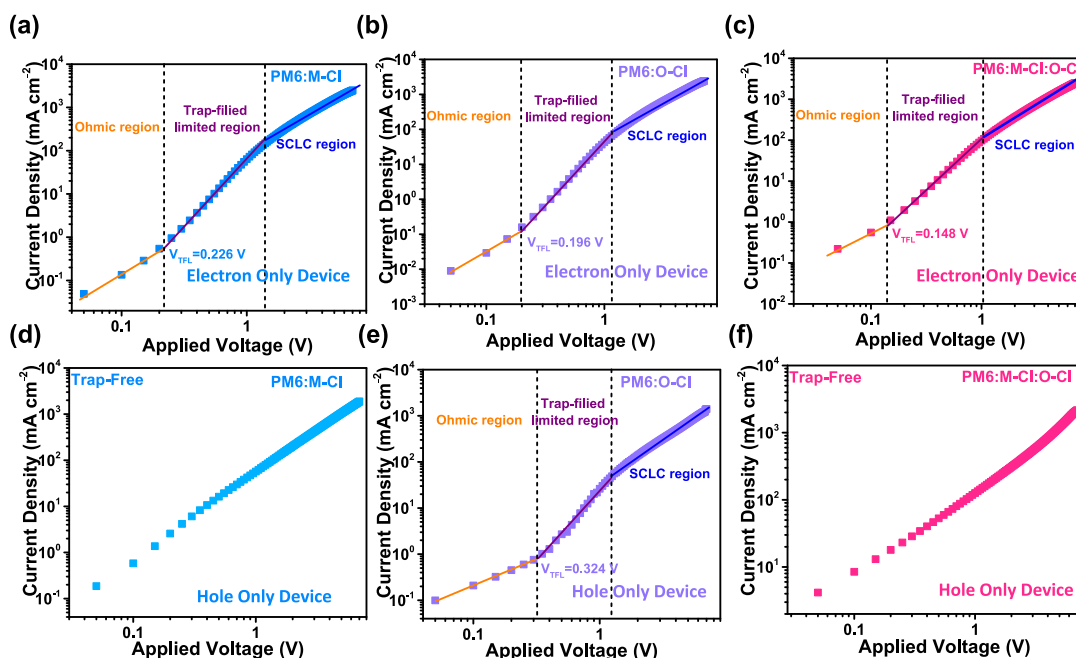


Fig. 6. (a), (b), and (c) The electron-only charge transport curves for PM6:M-Cl, PM6:O-Cl, and PM6:M-Cl:O-Cl devices; (d), (e) and (f) The hole-only charge transport curves for PM6:M-Cl, PM6:O-Cl and PM6:M-Cl:O-Cl devices.

PM6:O-Cl, and PM6:M-Cl:O-Cl devices as a function of $1/T^2$. The PM6:M-Cl:O-Cl device exhibits a σ_e value of 8.0 meV and σ_h value of 9.5 meV. Whereas the PM6:M-Cl device and the PM6:O-Cl device all present higher values as shown in Fig. 5i ($\sigma_e = 13.4$ meV, $\sigma_h = 11.4$ meV for PM6:M-Cl, $\sigma_e = 13.1$ meV, $\sigma_h = 20.0$ meV for PM6:O-Cl). The results indicate that the density of states (DoS) in the PM6:M-Cl:O-Cl device is narrower than in the other devices. Fig. S8 displays the energy disorder obtained by fitting the Fourier transform photocurrent quantum efficiency (FTPS-EQE) [64,65]. The PM6:M-Cl:O-Cl, PM6:O-Cl, and PM6:M-Cl devices exhibit energy disorders of 22.4 meV, 24.9 meV, and 23.2 meV, respectively. Although these values are higher than those obtained from mobility measurements, the ternary device exhibits the lowest energy disorder with both methods. Therefore, the trend with and without the third component may be more crucial in understanding the variations in device performance, rather than the absolute values. This feature is consistent with the reduced trap-assisted charge recombination and photo-CELIV results, suggesting that this isomer manipulate strategy can suppress both electron and hole energetic disorder in the active layer, thus fewer traps at the tails of the DoS, leading to the enhanced J_{SC} of and FF in the ternary devices.

The trap density variations were further confirmed by analyzing the J - V curves of electron-and hole-only devices (Fig. 6). The devices of PM6:M-Cl, PM6:O-Cl, and PM6:M-Cl:O-Cl exhibit different trap-filled limit voltage (V_{TFL}), where the V_{TFL} values of PM6:M-Cl:O-Cl devices in electron-only are 0.148 V and hole-only devices are none, corresponding to electron trap densities of $2.55 \times 10^{15} \text{ cm}^{-3}$ (hole trap densities is trap-free), lower than the electron trap densities of $3.89 \times 10^{15} \text{ cm}^{-3}$ (hole trap densities is trap-free) ($V_{TFL}(\text{electron}) = 0.226 \text{ V}$, $V_{TFL}(\text{hole})$ is None) for PM6:M-Cl device, and $3.37 \times 10^{15} \text{ cm}^{-3}$ and $5.58 \times 10^{15} \text{ cm}^{-3}$ ($V_{TFL}(\text{electron}) = 0.196 \text{ V}$, $V_{TFL}(\text{hole}) = 0.324 \text{ V}$) for PM6:O-Cl devices. Based on these results, we confirmed that the isomer acceptor is beneficial in reducing PM6:M-Cl:O-Cl device trap density and improving carrier mobilities. The reduction of trap density greatly inhibits trap recombination and promotes trap charge transport.

3. Conclusions

In summary, we presented a systematical study of the impact of

surface energy in ternary OSCs based on Y6 derivatives having different Cl substitution positions when paired with PM6 as a donor polymer. We could tune the surface energy of thin films by changing the M-Cl/O-Cl compositions, and the miscibility of materials dictates its influence. In addition, the PCE of ternary OSCs composed of PM6 and the M-Cl/O-Cl blend improves from 17% (PM6:M-Cl) to 18.1%. We found that the enhanced PCE is originally from the suppressed energy disorder, reduced trap density, and thus suppressed charge recombination, resulting from the more appropriate donor/acceptor phase separation morphology harmonized by tuning the thin film surface energy. Our findings on isomeric acceptors composition engineering provide a practical approach to managing the thin film surface energy for high-performed ternary OSCs and guidelines to exploit the potential of photovoltaic materials.

Declaration of Competing Interest

The authors declare that they have no known competing financial interests or personal relationships that could have appeared to influence the work reported in this paper.

Data availability

No data was used for the research described in the article.

Acknowledgements

S. Lu thanks the research grant from Chongqing Funds for Distinguished Young Scientists (cstc2020jcyj-jqx0018), Chongqing talent plan (CQYC201903008), and General Program of National Natural Science Foundation of China (62074149). Z. Kan acknowledges the support from the National Natural Science Foundation of China (No. 62275057), Guangxi Natural Science Foundation (2022GXNSFDA035066), and Guangxi University (A3120051029). H. Hu thanks the support from Scientific Research Startup Fund for Shenzhen High-Caliber Personnel of Shenzhen Polytechnic (No. 6022310038k and 6022310049k), the National Natural Science Foundation of China (No. 62004129) and Shenzhen Science and Technology Innovation Commission (Project No.

JCYJ20200109105003940). J. Lv thanks the support from China Postdoctoral Science Foundation (2022M720156). H. Chen thanks the support from Natural Science Foundation of China (22109157) and Youth Innovation Promotion Association Chinese Academy of Sciences (2020379). Special thanks to Dr. Deng for his help in energy loss testing and analysis. The authors thank Mr. Sein Chung in Prof. Kilwon Cho's group for his help on GIWAXS measurements, which were carried out at the 3C SAXS-I and 9A U-SAXS beamlines of Pohang Accelerator Laboratory (PLS-II), the Republic of Korea.

Appendix A. Supplementary data

Supplementary data to this article can be found online at <https://doi.org/10.1016/j.cej.2023.142822>.

References

- [1] Z. Luo, Y. Gao, H. Lai, Y. Li, Z. Wu, Z. Chen, R. Sun, J. Ren, C. Zhang, F. He, HanYoung Woo, J. Min, C. Yang, Asymmetric side-chain substitution enables a 3D network acceptor with hydrogen bond assisted crystal packing and enhanced electronic coupling for efficient organic solar cells, *Energy Environ. Sci.* 15 (11) (2022) 4601–4611, <https://doi.org/10.1039/D2EE01848A>.
- [2] J. Wu, M. Gao, Y. Chai, P. Liu, B. Zhang, J. Liu, L. Ye, Towards a bright future: the versatile applications of organic solar cells, *Mater. Rep. Energy* 1 (4) (2021), 100062, <https://doi.org/10.1016/j.matre.2021.100062>.
- [3] T.-P. Huynh, H. Haick, Autonomous flexible sensors for health monitoring, *Adv. Mater.* 30 (50) (2018) 1802337, <https://doi.org/10.1002/adma.201802337>.
- [4] D. Wang, H. Liu, Y. Li, G. Zhou, L. Zhan, H. Zhu, X. Lu, H. Chen, C.-Z. Li, High-performance and eco-friendly semitransparent organic solar cells for greenhouse applications, *Joule* 5 (4) (2021) 945–957, <https://doi.org/10.1016/j.joule.2021.02.010>.
- [5] Z. Zheng, J. Wang, P. Bi, J. Ren, Y. Wang, Y. Yang, X. Liu, S. Zhang, J. Hou, Tandem organic solar cell with 20.2% efficiency, *Joule* 6 (1) (2022) 171–184, <https://doi.org/10.1016/j.joule.2021.12.017>.
- [6] Y. Cui, H. Yao, J. Zhang, K. Xian, T. Zhang, L. Hong, Y. Wang, Y. Xu, K. Ma, C. An, C. He, Z. Wei, F. Gao, J. Hou, Single-junction organic photovoltaic cells with approaching 18% efficiency, *Adv. Mater.* 32 (19) (2020) 1908205, <https://doi.org/10.1002/adma.201908205>.
- [7] Y. Cui, Y. Xu, H. Yao, P. Bi, L. Hong, J. Zhang, Y. Zu, T. Zhang, J. Qin, J. Ren, Z. Chen, C. He, X. Hao, Z. Wei, J. Hou, Single-junction organic photovoltaic cell with 19% efficiency, *Adv. Mater.* 33 (41) (2021) 2102420, <https://doi.org/10.1002/adma.202102420>.
- [8] C. Li, J. Zhou, J. Song, J. Xu, H. Zhang, X. Zhang, J. Guo, L. Zhu, D. Wei, G. Han, J. Min, Y. Zhang, Z. Xie, Y. Yi, H. Yan, F. Gao, F. Liu, Y. Sun, Non-fullerene acceptors with branched side chains and improved molecular packing to exceed 18% efficiency in organic solar cells, *Nat. Energy* 6 (6) (2021) 605–613, <https://doi.org/10.1038/s41560-021-00820-x>.
- [9] X. Li, Q. Zhang, J. Yu, Y. Xu, R. Zhang, C. Wang, H. Zhang, S. Fabiano, X. Liu, J. Hou, F. Gao, M. Fahlman, Mapping the energy level alignment at donor/acceptor interfaces in non-fullerene organic solar cells, *Nat. Commun.* 13 (1) (2022) 2046, <https://doi.org/10.1038/s41467-022-29702-w>.
- [10] L. Hou, J. Lv, F. Wobben, V.M. Le Corre, H. Tang, R. Singh, M. Kim, F. Wang, H. Sun, W. Chen, Z. Xiao, M. Kumar, T. Xu, W. Zhang, I. McCulloch, T. Duan, H. Xie, L.J.A. Koster, S. Lu, Z. Kan, Effects of fluorination on fused ring electron acceptor for active layer morphology, exciton dissociation, and charge recombination in organic solar cells, *ACS Appl. Mater. Inter.* 12 (50) (2020) 56231–56239, <https://doi.org/10.1021/acsami.0c16411>.
- [11] S. Li, L. Ye, W. Zhao, X. Liu, J. Zhu, H. Ade, J. Hou, Design of a new small-molecule electron acceptor enables efficient polymer solar cells with high fill factor, *Adv. Mater.* 29 (46) (2017) 1704051, <https://doi.org/10.1002/adma.201704051>.
- [12] S. Wilken, D. Scheunemann, S. Dahlström, M. Nyman, J. Parisi, R. Österbacka, How to Reduce Charge Recombination in Organic Solar Cells: There are Still Lessons to Learn from P3HT:PCBM, *Adv. Electron. Mater.* 7 (5) (2021) 2001056, <https://doi.org/10.1002/aeml.202001056>.
- [13] D. Bartsaghi, I.D.C. Pérez, J. Kniepert, S. Roland, M. Turbiez, D. Neher, L.J.A. Koster, Competition between recombination and extraction of free charges determines the fill factor of organic solar cells, *Nat. Commun.* 6 (1) (2015), <https://doi.org/10.1038/ncomms8083>.
- [14] L. Xue, X. Liu, Q. Wang, M. Yang, S. Du, C. Yang, J. Tong, Y. Xia, J. Li, Improved Performance of Organic Solar Cells by Utilizing Green Non-Halogen Additive to Modulate Active-Layer Morphology, *Energy Technol.* n/a(n/a) (2022) 2200504, <https://doi.org/10.1002/ente.202200504>.
- [15] S. Bao, H. Yang, H. Fan, J. Zhang, Z. Wei, C. Cui, Y. Li, Volatilizable solid additive-assisted treatment enables organic solar cells with efficiency over 18.8% and fill factor exceeding 80%, *Adv. Mater.* 33 (48) (2021) 2105301, <https://doi.org/10.1002/adma.202105301>.
- [16] C. Li, X. Gu, Z. Chen, X. Han, N. Yu, Y. Wei, J. Gao, H. Chen, M. Zhang, A. Wang, J. Zhang, Z. Wei, Q. Peng, Z. Tang, X. Hao, X. Zhang, H. Huang, Achieving Record-Efficiency Organic Solar Cells upon Tuning the Conformation of Solid Additives, *J. Am. Chem. Soc.* 144 (32) (2022) 14731–14739, <https://doi.org/10.1021/jacs.2c05303>.
- [17] J. Song, L. Zhu, C. Li, J. Xu, H. Wu, X. Zhang, Y. Zhang, Z. Tang, F. Liu, Y. Sun, High-efficiency organic solar cells with low voltage loss induced by solvent additive strategy, *Matter* 4 (7) (2021) 2542–2552, <https://doi.org/10.1016/j.matt.2021.06.010>.
- [18] H.-C. Liao, C.-C. Ho, C.-Y. Chang, M.-H. Jao, S.B. Darling, W.-F. Su, Additives for morphology control in high-efficiency organic solar cells, *Mater. Today* 16 (9) (2013) 326–336, <https://doi.org/10.1016/j.mattod.2013.08.013>.
- [19] T. Xu, J. Lv, K. Yang, Y. He, Q. Yang, H. Chen, Q. Chen, Z. Liao, Z. Kan, T. Duan, K. Sun, J. Ouyang, S. Lu, 15.8% Efficiency binary all-small-molecule organic solar cells enabled by a selenophene substituted sematic liquid crystalline donor, *Energy Environ. Sci.* 14 (10) (2021) 5366–5376, <https://doi.org/10.1039/D1EE01193F>.
- [20] Q. Liu, Y. Jiang, K. Jin, J. Qin, J. Xu, W. Li, J. Xiong, J. Liu, Z. Xiao, K. Sun, S. Yang, X. Zhang, L. Ding, 18% Efficiency organic solar cells, *Sci. Bull.* 65 (4) (2020) 272–275, <https://doi.org/10.1016/j.scib.2020.01.001>.
- [21] Z. Zhou, S. Xu, J. Song, Y. Jin, Q. Yue, Y. Qian, F. Liu, F. Zhang, X. Zhu, High-efficiency small-molecule ternary solar cells with a hierarchical morphology enabled by synergizing fullerene and non-fullerene acceptors, *Nat. Energy* 3 (11) (2018) 952–959, <https://doi.org/10.1038/s41560-018-0234-9>.
- [22] K. Sun, Z. Xiao, S. Lu, W. Zajackowski, W. Pisula, E. Hantsen, J.M. White, R. M. Williamson, J. Subbiah, J. Ouyang, A.B. Holmes, W.W.H. Wong, D.J. Jones, A molecular nematic liquid crystalline material for high-performance organic photovoltaics, *Nat. Commun.* 6 (1) (2015) 6013, <https://doi.org/10.1038/ncomms7013>.
- [23] G. Li, V. Shrotriya, J. Huang, Y. Yao, T. Moriarty, K. Emery, Y. Yang, High-efficiency solution processable polymer photovoltaic cells by self-organization of polymer blends, *Nat. Mater.* 4 (11) (2005) 864–868, <https://doi.org/10.1038/nmat1500>.
- [24] F. Zhao, C. Wang, X. Zhan, Morphology control in organic solar cells, *Adv. Energy Mater.* 8 (28) (2018) 1703147, <https://doi.org/10.1002/aenm.201703147>.
- [25] Y. Xie, W. Zhou, J. Yin, X. Hu, L. Zhang, X. Meng, Q. Ai, Y. Chen, Post-annealing to reduce the open-circuit voltage caused by solvent annealing in organic solar cells, *J. Mater. Chem. A* 4 (16) (2016) 6158–6166, <https://doi.org/10.1039/C6TA00835F>.
- [26] B. Kadem, A.K. Hassan, W. Cranton, Efficient P3HT:PCBM bulk heterojunction organic solar cells; effect of post deposition thermal treatment, *J. Mater. Sci. Mater. Electron.* 27 (2016) 7038–7048, <https://doi.org/10.1007/s10854-016-4661-8>.
- [27] O.M. Ntwaeaborwa, R. Zhou, L. Qian, S.S. Pitale, J. Xue, H.C. Swart, P. H. Holloway, Post-fabrication annealing effects on the performance of P3HT:PCBM solar cells with/without ZnO nanoparticles, *Phys. B Condens. Matter* 407 (10) (2012) 1631–1633, <https://doi.org/10.1016/j.physb.2011.09.103>.
- [28] A. Karki, J. Vollbrecht, A.L. Dixon, N. Schopp, M. Schrock, G.N.M. Reddy, T.-Q. Nguyen, Understanding the high performance of over 15% efficiency in single-junction bulk heterojunction organic solar cells, *Adv. Mater.* 31 (48) (2019) 1903868, <https://doi.org/10.1002/adma.201903868>.
- [29] H. Tang, T. Xu, C. Yan, J. Gao, H. Yin, J. Lv, R. Singh, M. Kumar, T. Duan, Z. Kan, S. Lu, G. Li, Donor derivative incorporation: an effective strategy toward high performance all-small-molecule ternary organic solar cells, *Adv. Sci.* 6 (21) (2019) 1901613, <https://doi.org/10.1002/advs.201901613>.
- [30] J. Lv, H. Tang, J. Huang, C. Yan, K. Liu, Q. Yang, D. Hu, R. Singh, J. Lee, S. Lu, G. Li, Z. Kan, Additive-induced miscibility regulation and hierarchical morphology enable 17.5% binary organic solar cells, *Energy Environ. Sci.* 14 (5) (2021) 3044–3052, <https://doi.org/10.1039/D0EE04012F>.
- [31] C. Yan, H. Tang, R. Ma, M. Zhang, T. Liu, J. Lv, J. Huang, Y. Yang, T. Xu, Z. Kan, H. Yan, F. Liu, S. Lu, G. Li, Synergy of liquid-crystalline small-molecule and polymeric donors delivers uncommon morphology evolution and 16.6% efficiency organic photovoltaics, *Adv. Sci.* 7 (15) (2020) 2000149, <https://doi.org/10.1002/advs.202000149>.
- [32] P. Bi, S. Zhang, Z. Chen, Y. Xu, Y. Cui, T. Zhang, J. Ren, J. Qin, L. Hong, X. Hao, J. Hou, Reduced non-radiative charge recombination enables organic photovoltaic cell approaching 19% efficiency, *Joule* 5 (9) (2021) 2408–2419, <https://doi.org/10.1016/j.joule.2021.06.020>.
- [33] L. Zhu, M. Zhang, J. Xu, C. Li, J. Yan, G. Zhou, W. Zhong, T. Hao, J. Song, X. Xue, Z. Zhou, R. Zeng, H. Zhu, C.C. Chen, R.C.I. MacKenzie, Y. Zou, J. Nelson, Y. Zhang, Y. Sun, F. Liu, Single-junction organic solar cells with over 19% efficiency enabled by a refined double-fibril network morphology, *Nat. Mater.* 21 (6) (2022) 656–663, <https://doi.org/10.1038/s41563-022-01244-y>.
- [34] P.W.M. Blom, V.D. Mihailescu, L.J.A. Koster, D.E. Markov, Device physics of polymer:fullerene bulk heterojunction solar cells, *Adv. Mater.* 19 (12) (2007) 1551–1566, <https://doi.org/10.1002/adfm.200601093>.
- [35] H. Fan, H. Yang, Y. Wu, O. Yildiz, X. Zhu, T. Marszalek, P.W.M. Blom, C. Cui, Y. Li, Anthracene-assisted morphology optimization in photoactive layer for high-efficiency polymer solar cells, *Adv. Funct. Mater.* 31 (37) (2021) 2103944, <https://doi.org/10.1002/adfm.202103944>.
- [36] T. Liu, W. Gao, Y. Wang, T. Yang, R. Ma, G. Zhang, C. Zhong, W. Ma, H. Yan, C. Yang, Unconjugated Side-Chain Engineering Enables Small Molecular Acceptors for Highly Efficient Non-Fullerene Organic Solar Cells: Insights into the Fine-Tuning of Acceptor Properties and Micromorphology, *Adv. Funct. Mater.* 29 (26) (2019) 1902155, <https://doi.org/10.1002/adfm.201902155>.
- [37] H. Yan, J.G. Manion, M. Yuan, F.P. Garcia de Arquer, G.R. McKeown, S. Beaupre, M. Leclerc, E.H. Sargent, D.S. Seferos, Increasing polymer solar cell fill factor by trap-filling with F4-TCNQ at parts per thousand concentration, *Adv. Mater.* 28 (30) (2016) 6491–6496, <https://doi.org/10.1002/adma.201601553>.
- [38] H. Yan, J. Chen, K. Zhou, Y. Tang, X. Meng, X. Xu, W. Ma, Lewis acid doping induced synergistic effects on electronic and morphological structure for donor and acceptor in polymer solar cells, *Adv. Energy Mater.* 8 (19) (2018) 1703672, <https://doi.org/10.1002/aenm.201703672>.

- [39] D. Li, F. Geng, T. Hao, Z. Chen, H. Wu, Z. Ma, Q. Xue, L. Lin, R. Huang, S. Leng, B. Hu, X. Liu, J. Wang, H. Zhu, M. Lv, L. Ding, M. Fahlman, Q. Bao, Y., Li, n-Doping of photoactive layer in binary organic solar cells realizes over 18.3% efficiency, *Nano Energy* 96 (2022), 107133, <https://doi.org/10.1016/j.nanoen.2022.107133>.
- [40] H. Feng, Y. Dai, L. Guo, D.i. Wang, H. Dong, Z. Liu, L.u. Zhang, Y. Zhu, C. Su, Y. Chen, W. Wu, Exploring ternary organic photovoltaics for the reduced non-radiative recombination and improved efficiency over 17.23% with a simple large-bandgap small molecular third component, *Nano Res.* 15 (4) (2022) 3222–3229, <https://doi.org/10.1007/s12274-021-3945-3>.
- [41] K. Chong, X. Xu, H. Meng, J. Xue, L. Yu, W. Ma, Q. Peng, Realizing 19.05% efficiency polymer solar cells by progressively improving charge extraction and suppressing charge recombination, *Adv. Mater.* 34 (13) (2022) 2109516, <https://doi.org/10.1002/adma.202109516>.
- [42] D. Hu, Q. Yang, H. Chen, F. Wobben, V.M. Le Corre, R. Singh, T. Liu, R. Ma, H. Tang, L.J.A. Koster, T. Duan, H.e. Yan, Z. Kan, Z. Xiao, S. Lu, 15.34% efficiency all-small-molecule organic solar cells with an improved fill factor enabled by a fullerene additive, *Energy Environ. Sci.* 13 (7) (2020) 2134–2141.
- [43] S. Pang, R. Zhang, C. Duan, S. Zhang, X. Gu, X. Liu, F. Huang, Y. Cao, Alkyl chain length effects of polymer donors on the morphology and device performance of polymer solar cells with different acceptors, *Adv. Energy Mater.* 9 (30) (2019) 1901740, <https://doi.org/10.1002/aenm.201901740>.
- [44] X. Liao, Q. He, G. Zhou, X. Xia, P. Zhu, Z. Xing, H. Zhu, Z. Yao, X. Lu, Y. Chen, Regulating favorable morphology evolution by a simple liquid-crystalline small molecule enables organic solar cells with over 17% efficiency and a remarkable Jsc of 26.56 mA/cm², *Chem. Mater.* 33(1) (2021) 430–440. <https://doi.org/10.1021/acs.chemmater.0c04297>.
- [45] H.B. Naveed, W. Ma, Miscibility-driven optimization of nanostructures in ternary organic solar cells using non-fullerene acceptors, *Joule* 2 (4) (2018) 621–641, <https://doi.org/10.1016/j.joule.2018.02.010>.
- [46] D. Baran, R.S. Ashraf, D.A. Hanifi, M. Abdelsamie, N. Gasparini, J.A. Röhr, S. Holliday, A. Wadsworth, S. Lockett, M. Neophytou, C.J.M. Emmott, J. Nelson, C. J. Brabec, A. Amassian, A. Salleo, T. Kirchartz, J.R. Durrant, I. McCulloch, Reducing the efficiency–stability–cost gap of organic photovoltaics with highly efficient and stable small molecule acceptor ternary solar cells, *Nat. Mater.* 16 (3) (2017) 363–369, <https://doi.org/10.1038/nmat4797>.
- [47] H. Lai, X. Lai, Z.-Y. Chen, Y. Zhu, H. Wang, H. Chen, P. Tan, Y. Zhu, Y. Zhang, F. He, Crystallography, Packing Mode, and Aggregation State of Chlorinated Isomers for Efficient Organic Solar Cells, *CCS Chem.* (2022) 1–12, <https://doi.org/10.31635/ccschem.022.202201875>.
- [48] H. Tang, J. Lv, K. Liu, Z. Ren, H.T. Chandran, J. Huang, Y. Zhang, H. Xia, J.I. Khan, D. Hu, C. Yan, J. Oh, S. Chen, S. Chu, P.W.K. Fong, H. Chen, Z. Xiao, C. Yang, Z. Kan, F. Laquai, S. Lu, G. Li, Self-assembly enables simple structure organic photovoltaics via green-solvent and open-air-printing: Closing the lab-to-fab gap, *Mater. Today* 55 (2022) 46–55, <https://doi.org/10.1016/j.mattod.2022.04.005>.
- [49] L. Zhang, N. Yi, W. Zhou, Z. Yu, F. Liu, Y. Chen, Miscibility tuning for optimizing phase separation and vertical distribution toward highly efficient organic solar cells, *Adv. Sci.* 6 (15) (2019) 1900565, <https://doi.org/10.1002/advs.201900565>.
- [50] T. Fukuhara, Y. Tamai, I. Osaka, H. Ohkita, Bimolecular recombination and fill factor in crystalline polymer solar cells, *Jpn. J. Appl. Phys.* 57 (8S3) (2018) 08RE01, <https://doi.org/10.7567/JJAP.57.08RE01>.
- [51] Z. Luo, R. Ma, J. Yu, H. Liu, T. Liu, F. Ni, J. Hu, Y. Zou, A. Zeng, C.-J. Su, U.-S. Jeng, X. Lu, F. Gao, C. Yang, H. Yan, Heteroheptacene-based acceptors with thieno[3,2-b]pyrrole yield high-performance polymer solar cells, *Nat. Sci. Rev.* 9(7) (2022). <https://doi.org/10.1093/nsr/nwac076>.
- [52] L. Lu, M.A. Kelly, W. You, L. Yu, Status and prospects for ternary organic photovoltaics, *Nat. Photon.* 9 (8) (2015) 491–500, <https://doi.org/10.1038/nphoton.2015.128>.
- [53] X. Liu, Y. Yan, Y. Yao, Z. Liang, Ternary Blend Strategy for Achieving High-Efficiency Organic Solar Cells with Nonfullerene Acceptors Involved, *Adv. Funct. Mater.* 28 (29) (2018) 1802004, <https://doi.org/10.1002/adfm.201802004>.
- [54] Y. Chen, P. Ye, Z.G. Zhu, X. Wang, L. Yang, X. Xu, X. Wu, T. Dong, H. Zhang, J. Hou, F. Liu, H. Huang, Achieving High-Performance Ternary Organic Solar Cells through Tuning Acceptor Alloy, *Adv. Mater.* 29 (6) (2017) 1603154, <https://doi.org/10.1002/adma.201603154>.
- [55] R. Yu, S. Zhang, H. Yao, B. Guo, S. Li, H. Zhang, M. Zhang, J. Hou, Two well-miscible acceptors work as one for efficient fullerene-free organic solar cells, *Adv. Mater.* 29 (26) (2017) 1700437, <https://doi.org/10.1002/adma.201700437>.
- [56] L. Zhan, S. Li, T.-K. Lau, Y. Cui, X. Lu, M. Shi, C.-Z. Li, H. Li, J. Hou, H. Chen, Over 17% efficiency ternary organic solar cells enabled by two non-fullerene acceptors working in an alloy-like model, *Energ. Environ. Sci.* 13 (2) (2020) 635–645, <https://doi.org/10.1039/C9EE03710A>.
- [57] L. Arunagiri, Z. Peng, X. Zou, H. Yu, G. Zhang, Z. Wang, J.Y. Lin Lai, J. Zhang, Y. Zheng, C. Cui, F. Huang, Y. Zou, K.S. Wong, P.C.Y. Chow, H. Ade, H.e. Yan, Selective Hole and Electron Transport in Efficient Quaternary Blend Organic Solar Cells, *Joule* 4 (8) (2020) 1790–1805, <https://doi.org/10.1016/j.joule.2020.06.014>.
- [58] G.F. Burkhard, E.T. Hoke, M.D. McGehee, Accounting for interference, scattering, and electrode absorption to make accurate internal quantum efficiency measurements in organic and other thin solar cells, *Adv. Mater.* 22 (30) (2010) 3293–3297, <https://doi.org/10.1002/adma.201000883>.
- [59] Y. Gong, Z. Kan, W. Xu, Y. Wang, S.H. Alshammari, F. Laquai, W.-Y. Lai, W. Huang, Wide-Bandgap Small Molecular Acceptors Based on a Weak Electron-Withdrawing Moiety for Efficient Polymer Solar Cells, *Sol. RRL* 2 (10) (2018) 1800120, <https://doi.org/10.1002/solr.201800120>.
- [60] A.J. Mozer, G. Dennler, N.S. Sariciftci, M. Westerling, A. Pivrikas, R. Österbacka, G. Juska, Time-dependent mobility and recombination of the photoinduced charge carriers in conjugated polymer/fullerene bulk heterojunction solar cells, *Phys. Rev. B* 72 (3) (2005), 035217, <https://doi.org/10.1103/PhysRevB.72.035217>.
- [61] A. Pivrikas, G. Juska, A.J. Mozer, M. Scharber, K. Arlauskas, N.S. Sariciftci, H. Stubb, R. Osterbacka, Bimolecular recombination coefficient as a sensitive testing parameter for low-mobility solar-cell materials, *Phys. Rev. Lett.* 94 (17) (2005), 176806, <https://doi.org/10.1103/PhysRevLett.94.176806>.
- [62] Y. Liu, Y. Gao, B. Xu, P.H.M. van Loosdrecht, W. Tian, Trap-limited bimolecular recombination in poly(3-hexylthiophene): Fullerene blend films, *Org. Electron.* 38 (2016) 8–14, <https://doi.org/10.1016/j.orgel.2016.07.018>.
- [63] J. Guo, H. Ohkita, S. Yokoya, H. Bentes, S. Ito, Bimodal polarons and hole transport in poly(3-hexylthiophene):fullerene blend films, *J. Am. Chem. Soc.* 132 (28) (2010) 9631–9637, <https://doi.org/10.1021/ja9108787>.
- [64] S. Liu, J. Yuan, W. Deng, M. Luo, Y. Xie, Q. Liang, Y. Zou, Z. He, H. Wu, Y. Cao, High-efficiency organic solar cells with low non-radiative recombination loss and low energetic disorder, *Nat. Photon.* 14 (5) (2020) 300–305, <https://doi.org/10.1038/s41566-019-0573-5>.
- [65] Z. Luo, T. Liu, Y. Wang, G. Zhang, R. Sun, Z. Chen, C. Zhong, J. Wu, Y. Chen, M. Zhang, Y. Zou, W. Ma, H. Yan, J. Min, Y. Li, C. Yang, Reduced energy loss enabled by a chlorinated thiophene-fused ending-group small molecular acceptor for efficient nonfullerene organic solar cells with 13.6% efficiency, *Adv. Energy Mater.* 9 (18) (2019) 1900041, <https://doi.org/10.1002/aenm.201900041>.